7 Tesla MRI of the *ex vivo* human brain at 100 micron resolution

Brian L. Edlow[1,2], Azma Mareyam[2], Andreas Horn[3], Jonathan R. Polimeni[2], M. Dylan Tisdall[4], Jean Augustinack[2], Jason P. Stockmann[2], Bram R. Diamond[2], Allison Stevens[2], Lee S. Tirrell[2], Rebecca D. Folkerth[5], Lawrence L. Wald[2], Bruce Fischl[2,*] & Andre van der Kouwe[2,*]

* co-senior authors

1. Center for Neurotechnology and Neurorecovery, Massachusetts General Hospital, Department of Neurology, Boston, MA 02114, USA

2. Athinoula A. Martinos Center for Biomedical Imaging, Massachusetts General Hospital, Department of Radiology, Charlestown, MA 02129, USA

3. Movement Disorders & Neuromodulation Section, Department for Neurology, Charité – University Medicine Berlin, Germany

4. Radiology, Perelman School of Medicine, University of Pennsylvania, Philadelphia, PA 19104, USA

5. City of New York Office of the Chief Medical Examiner, and New York University School of Medicine, New York, NY, USA

corresponding author: Brian Edlow (bedlow@mgh.harvard.edu)

Abstract

We present an ultra-high resolution MRI dataset of an *ex vivo* human brain specimen. The brain specimen was donated by a 58-year-old woman who had no history of neurological disease and died of non-neurological causes. After fixation in 10% formalin, the specimen was imaged on a 7 Tesla MRI scanner at 100 µm isotropic resolution using a custom-built 31-channel receive array coil. Single-echo multi-flip Fast Low-Angle SHot (FLASH) data were acquired over 100 hours of scan time (25 hours per flip angle), allowing derivation of a T1 parameter map and synthesized FLASH volumes. This dataset provides an unprecedented view of the three-dimensional neuroanatomy of the human brain. To optimize the utility of this resource, we warped the dataset into standard stereotactic space. We now distribute the dataset in both native space and stereotactic space to the academic community via multiple platforms. We envision that this dataset will have a broad range of investigational, educational, and clinical applications that will advance understanding of human brain anatomy in health and disease.

Design Type(s)	Single measure design
Measurement Type(s)	Nuclear magnetic resonance assay
Technology Type(s)	7 Tesla MRI scanner
Factor Type(s)	
Sample Characteristic(s)	Homo sapiens • brain

Background & Summary

Postmortem *ex vivo* MRI provides significant advantages over *in vivo* MRI for visualizing the microstructural neuroanatomy of the human brain. Whereas *in vivo* MRI acquisitions are constrained by time (i.e. ~hours) and affected by motion, *ex vivo* MRI can be performed without time constraints (i.e. ~days) and without cardiorespiratory or head motion. The resultant advantages for characterizing neuroanatomy at microscale are particularly important for identifying cortical layers and subcortical nuclei[1-5], which are difficult to visualize even in the highest-resolution *in vivo* MRI datasets[6,7]. *Ex vivo* MRI also provides advantages over histological methods that are associated with distortion and tearing of human brain tissue during fixation, embedding, and slide-mounting.

As the field of *ex vivo* MRI has developed over the past two decades, several laboratories have focused on imaging blocks of tissue from human brain specimens using small-bore scanners[2,8] and specialized receive coils[9-11]. This approach allows for spatial resolutions of up to 35–75 microns for analyses of specific neuroanatomic regions[9,11-13]. However, ultra-high resolution imaging of whole human brain specimens at high magnetic field strengths has been far more challenging, due to the need for multi-channel receive coils and large-bore clinical scanners that can accommodate a whole-brain specimen. Whole-brain imaging is required to observe neuroanatomic relationships across distant brain regions, as well as to provide a complete view of human neuroanatomy in standard stereotactic space.

Here, we report the results of a multidisciplinary effort to image a whole human brain specimen *ex vivo* at an unprecedented spatial resolution of 100

64   µm isotropic.   Central to this effort was the construction of an integrated

65   system consisting of a custom-built 31-channel receive array coil and volume

66   transmit coil, which was designed to accommodate and tightly enclose an *ex*

67   *vivo* human brain[14].   The scans were performed on a 7 Tesla whole-body

68   human MRI scanner using four single-echo spoiled gradient-recalled echo

69   (SPGR/GRE) or Fast Low-Angle SHot (FLASH) sequences. We used varying

70   flip-angles (FA15°, FA20°, FA25°, FA30°) to generate multiple synthesized

71   volumes, each of which provides a different tissue contrast.   The scans,

72   performed over ~100 hours (~25 hours per FA), generated an ~8 TB dataset

73   (~2 TB per flip angle) that required custom-built computational tools for offline

74   MRI reconstruction and creation of the synthesized volumes.   Offline MRI

75   reconstruction considerably reduces the data amount.   We release the

76   resulting FA25° acquisition, as well as the synthesized FLASH25 volume here,

77   both in native space and coregistered to standard stereotactic space, for use

78   by the academic community. We envision a broad range of investigational,

79   educational, and clinical applications for this dataset that have the potential to

80   advance understanding of human brain anatomy in health and disease.

81

82   **Methods**

83   **Specimen acquisition and processing**

84   A 58-year-old woman with a history of lymphoma and stem cell

85   transplantation, but no history of neurological or psychiatric disease, died in a

86   medical intensive care unit.   She was initially admitted to the hospital for

87   fevers, chills, and fatigue, and then was transferred to the intensive care unit

88   for hypoxic respiratory failure requiring mechanical ventilation.   Her hospital

89   course was also notable for a deep venous thromboses and a pulmonary

90   embolism. The cause of her death on hospital day 15 was determined to be

91   hypoxic respiratory failure due to viral pneumonia. At the time of her death,

92   her surrogate decision-maker provided written informed consent for a clinical

93   autopsy and for donation of her brain for research, as part of a protocol

94   approved by our Institutional Review Board.

95   At autopsy, her fresh brain weighed 1,210 grams (normal range = 1,200

96   to 1,500 grams). The brain was fixed in 10% formalin 14 hours after death.

97   Gross examination revealed a normal brain (Fig. 1), without evidence of mass

98   lesions or cerebrovascular disease. To ensure adequate fixation and prevent

99   specimen flattening (which can prevent specimens from fitting into custom *ex*

100   *vivo* MRI coils), we followed a series of standard specimen processing

101   procedures, as previously described[15].

102

103   **Specimen preparation for scanning**

104   After remaining in fixative for 35 months, the brain specimen was transferred

105   to Fomblin Y LVAC 06/6 (perfluoropolyether, Solvay Specialty Polymers USA,

106   LLC, West Deptford, NJ), which is invisible to MR and reduces magnetic

107   susceptibility artifacts.   The specimen, immersed in Fomblin, was then

108   secured inside a custom-built, air-tight brain holder made of rugged

109   urethane[16]. The brain holder contains degassing ports for removal of air

110   bubbles, which further reduces magnetic susceptibility artifacts.

111

112   **Construction of a receive array coil and transmit volume coil for *ex vivo***

113   **imaging of the whole human brain**

114   We built a receive coil apparatus consisting of a 31-channel surface coil loop

115   array with two halves. The apparatus was fabricated using a 3D printer of

116 slightly larger dimensions than the brain holder, which slides inside the single-

117 channel birdcage volume transmit coil (Fig. 2). The brain holder is an oblate

118 spheroid (16 × 19 cm) that conforms to the shape of a whole brain (cerebral

119 hemispheres + cerebellum + brainstem)[16] (Fig. 2d). It is made of two separate

120 halves that can be sealed together with a silicone gasket after packing the

121 brain inside. This holder must also withstand the degassing process when

122 under vacuum pressure. Degassing is performed in three steps: 1) introducing

123 vacuum suction into the container with the brain inside, which allows the

124 bubbles to expand under decreased pressure and exit tissue cavities; 2)

125 opening the valve to fill the holder with fomblin and then sealing off the fill

126 valve; and 3) continuation of vacuum suction with low-amplitude vibration of

127 the holder for 2-6 hours. The vibration facilitates the removal of bubbles from

128 tissue cavities. All three steps are performed inside a fume hood.

129   The coil former (Fig. 2c) consists of two halves and encloses the brain

130 holder. The receive array coil consists of 31 detectors (Fig. 2a), with 15

131 elements on the top half (diameter = 5.5 cm) and 16 on the bottom half

132 (diameter = 8.5 cm). Coil elements were constructed using 16 AWG wire

133 loops [17], each with four or five evenly spaced capacitors (Supplementary Fig.

134 1). All elements were tuned to 297.2 MHz and matched to a loaded

135 impedance of 75 Ω to minimize preamplifier noise. Preamplifier decoupling

136 was achieved with a cable length of 6 cm. Preamplifiers were placed directly

137 on the coil elements, yielding a substantial reduction in cable losses compared

138 to a previous 30-channel *ex vivo* brain array[18]. The active detuning circuit was

139 formed across the match capacitor using an inductor and PIN diode.

140   Tuning, matching, and decoupling of neighboring elements was

141 optimized on the bench with a brain sample immersed in periodate-lysine-

142 paraformaldehyde (PLP) solution. Because coil loading varies with the fixative

143 used, the coil must be tuned and matched on the bench using a brain sample

144 with the correct fixative. (For example, testing can be performed with a brain

145 sample immersed in PLP or formalin, but not the regular loading phantom

146 comprised of water and salt). Loops tuned/matched on PLP showed

147 unloaded-to-loaded quality factor ratio (Q-ratio) of Q_{UL}/Q_L = 210/20 = 10.5,

148 corresponding to an equivalent noise resistance of 11 ohms for the loaded coil

149 (Q = wL/R). By contrast, formalin is a less lossy fixative, giving a coil Q-ratio

150 of Q_{UL}/Q_L = 210/60 = 3.5, corresponding to an equivalent noise resistance of 4

151 ohms.

152   A shielded detunable volume coil (Fig. 2) was built for excitation, with

153 the following parameters and features: band-pass birdcage, diameter 26.7 cm,

154 and an extended length of 32 cm to accommodate brain samples of larger

155 dimensions. For the detuning circuit we used diodes in every leg of the

156 birdcage. These diodes are powered with the high-power chokes, which can

157 withstand high voltage and short duration inversion pulses.

158   In summary, this coil system incorporates an improved mechanical

159 design, preamps mounted at the coil detectors, and an extended transmit coil

160 design capable of producing high-power pulses.

161

162 **7 Tesla MRI data acquisition**

163 The brain specimen was scanned on a whole-body human 7 Tesla (7T)

164 Siemens Magnetom MRI scanner (Siemens Healthineers, Erlangen,

165 Germany) with the custom-built coil described above. We utilized a GRE

166 sequence[19] at 100 μm isotropic spatial resolution with the following acquisition

167 parameters: TR = 40 msec, TE = 14.2 msec, bandwidth = 90 Hz/px, FA = 15˚,

168   20°, 25°, 30°. Total scan time for each FA was 25:01:52 [hh:mm:ss], and each

169   FA acquisition generated 1.98 TB of raw k-space data. To improve the signal-

170   to-noise ratio (SNR) and optimise T_1 modelling, we collected FLASH scans at

171   four FAs: 15°, 20°, 25°, 30° (Fig. 3). Accounting for localizers, quality

172   assurance (QA) scans, and adjustment scans, the total scan time was 100

173   hours and 8 minutes, and we collected nearly 7.92 TB of raw k-space data.

174

175   **MRI data reconstruction**

176   The size of the k-space data exceeded the storage capacity of the RAID

177   provided by the scanner image reconstruction computer.   The image

178   reconstruction also required more RAM than what was available.   We

179   therefore implemented software on the scanner to stream the data directly

180   via TCP/IP to a server on an external computer added to the scanner network,

181   which saved the data as they were received. Because of additional limitations

182   related to the total size of the raw data for any single scan, as dictated by the

183   imager RAID size, we also divided each acquisition into segments.   The

184   server on the external computer stored the data as they were acquired,

185   creating date stamps for every k-space segment.

186   After the scan was completed, the streamed k-space data were

187   transferred to a computational server where we ran custom software to stitch

188   together the segments, reconstruct the images for each channel (via a 3D FFT

189   on each volume per channel[20]), and combine the images derived from the 31

190   channels via the root-sum-of-squares of the signal magnitudes at each voxel.

191   These signal magnitudes were channel-wise decorrelated using a covariance

192   matrix of the channels' thermal noise. The output from coil combination was

193   the final acquired image (Data Citation 1; Videos 1, 2 and 3).

194

MRI data processing

The acquired data underwent a series of processing steps, culminating in the creation of a T_1 parameter map and synthesized FLASH volumes (Fig. 3 and Fig. 4; Videos 4, 5, and 6; Data Citations 1 and 2). The volumes were estimated directly from the four FLASH acquisitions using the DESPOT1 algorithm[19,21] with the program 'mri_ms_fitparms' distributed in FreeSurfer (http://surfer.nmr.mgh.harvard.edu) to quantify tissue properties independent of scanner and sequence types. This algorithm fits the tissue parameters (i.e. T1) of the signal equation for the FLASH scan at each voxel using multiple input volumes. The volumes at the originally acquired TRs and flip angles were then regenerated from the parameter maps by evaluating the FLASH signal equation. In principle, a volume with any TR and flip angle combination could be synthesized. These synthesized volumes are created from all the acquired data, and therefore have better SNR than the individually acquired input volumes. We choose to release the 25 degree synthetic volume as it has maximal SNR and the best apparent contrast for cortical and subcortical structures[9].

Of note, *ex vivo* MRI of the fixed human brain yields a different contrast than *in vivo* MRI, mainly from a shortened T_1, but also from a decrease in T_2^*, both of which are related to formalin fixation[22]. The predominant source of signal contrast in *ex vivo* MRI is likely myelin[23] and/or iron[24]. Specifically, myelin appears to be a source of T_1 contrast, while cortical iron appears to be a source of T_2^* contrast[25].

218

Coregistration of the dataset to standard stereotactic space

9

220 The dataset was spatially normalized into the MNI ICBM 2009b NLIN ASYM

221 template[26] (Supplementary Fig. 2a). This template constitutes the newest

222 version of the "MNI space" and is considered a high-resolution version of MNI

223 space because it is available at 0.5 mm isotropic resolution. To combine

224 structural information present on T_1 and T_2 versions of the template, we

225 created a joint template using PCA, as previously described[27]. The four

226 synthesized FLASH volumes (FA15, FA20, FA25, and FA30) were

227 downsampled to isotropic voxel-sizes of 0.5 mm for spatial normalization and

228 initially registered into template space in a multispectral approach using

229 Advanced Normalization Tools (ANTs; http://stnava.github.io/ANTs/; [28]). This

230 multispectral approach simultaneously accounts for intensity data in all four

231 volumes. The initial normalization was performed in four stages (rigid body,

232 affine, whole brain SyN and subcortically focused SyN) as defined in the

233 "effective: low variance + subcortical refine" preset implemented in Lead-DBS

234 software (www.lead-dbs.org; [29]).

235   To refine the warp, we introduced fiducial regions of interest (ROI)

236 iteratively using a tool developed for this task (available within Lead-DBS).

237 Specifically, we manually drew line and point fiducial markers in both native

238 and template spaces (Supplementary Fig. 2b). In addition, we manually

239 segmented four structures in native space (subthalamic nucleus, internal and

240 external pallidum and red nucleus). The three types of fiducials (line ROI,

241 spherical ROI and manual segmentations of key structures) were then added

242 as "spectra" in subsequent registration refinements (Supplementary Fig. 2c).

243 Thus, the final registration consisted of a large number of pairings between

244 native and template space (the first four being the actual anatomical volumes,

245 the subsequent ones being manual segmentations and paired helper

246 fiducials). To achieve maximal registration precision, the warp was refined in

247 over 30 iterations with extensive manual expert interaction, each refinement

248 continuing directly from the last saved state. We used linear interpolation to

249 create the normalized files in the data release (Data Citations 1 and 3).

250

251 **Code availability**

252 Neuroimaging data were processed using standard processing pipelines

253 (http://surfer.nmr.mgh.harvard.edu/, https://github.com/freesurfer/freesurfer).

254 All code used for registration of volumes into standard stereotactic space are

255 available within the open-source Lead-DBS software

256 (https://github.com/leaddbs/leaddbs). Because registration involved multiple

257 manual user interface steps, no ready-made code is provided, but the process

258 can be readily reproduced with the provided data and software.

259

260 **Data Records**

261 The native space FA25° acquisition and synthesized FLASH25 volume are

262 available for download at https://datadryad.org (Data Citation 1). Additional

263 synthesized volumes are available upon request to the corresponding author.

264 Axial, coronal, and sagittal videos of the native space FA25° acquisition

265 (Videos 1, 2, and 3) and synthesized FLASH25 volume (Videos 4, 5, and 6)

266 are also available at the Dryad data repository (Data Citation 1). The

267 synthesized FLASH25 volume is available for interactive, online viewing at

268 https://histopath.nmr.mgh.harvard.edu (Data Citation 2). The normalized

269 FLASH25 volume in standard stereotactic space is available at the Dryad data

270 repository (Data Citation 1) and is hosted on www.lead-dbs.org (preinstalled

271 as part of the LEAD-DBS software package; Data Citation 3).

11

272

Technical Validation

Coil signal-to-noise ratio (SNR) measurements

The receive coil has a Q_{UL}/Q_L ratio that ranged from 6 in the top half elements to 8 in the bottom half elements due to larger coil diameter. The S_{12} coupling between neighbouring elements, measured with all other coils active detuned, ranged from −10.9 to −24 dB. All individual elemnts had $S_{11} <$ −20 dB and active detuning of > 30 dB. We evaluated the performance of the transmit coil by examining the B_1^+ profile[14], which shows the efficiency throughout the entire spatial distribution of the brain specimen. The efficiency was greatest in the center of the specimen and fell off gradually towards the edges, as expected for a whole brain specimen at 7T.

We compared the SNR of the 31-channel *ex vivo* array to that of a standard 31-channel 7T head coil and a 64-channel 3T head coil. SNR maps were computed following the method of Kellman & McVeigh[30]. We calibrated the voltage required for 180° pulse using a B_1^+ map (estimated with the AFI method)[31] with an ROI of 3-cm diameter at the center of the brain. We estimated array noise covariance from thermal noise data acquired without RF excitation. The SNR gain with the 31-channel *ex vivo* array was 1.6-fold versus the 31-channel 7T standard coil and 3.3-fold versus the 64-channel 3T head array (Fig. 5). The noise coupling between channels was 11% for the 31-channel *ex vivo* array, a 2-fold improvement relative to our previous array[18].

295

Coregistration accuracy

297   We assessed the neuroanatomic accuracy of the final registration results (i.e.

298   the fit between structures on the normalized FLASH volumes versus the high-

299   resolution MNI template) by visual inspection using a tool specifically designed

300   for this task (implemented in Lead-DBS). An example of this visual inspection

301   assessment for the subthalamic nucleus and globus pallidus interna is

302   provided in Supplementary Fig. 3. The final maps are stored in NIfTI and mgz

303   files in isotropic 150 µm resolution (Data Citation 1). The normalized

304   FLASH25 volume is additionally distributed pre-installed within Lead-DBS

305   software and can be selected for visualization in the 3D viewer (Data Citation

306   3). Fig. 6 shows an example in synopsis with deep brain stimulation electrode

307   reconstructions in a hypothetical patient being treated for Parkinson's

308   Disease.

Acknowledgements

334   as well as the German Research Foundation (Emmy Noether Grant

335   410169619).

336

Author contributions

B.L.E. designed the study, analyzed the data, and prepared the manuscript.

A.M. built the coil, acquired and analyzed the data, and contributed to the manuscript.

A.H. created the warp from native space to standard stereotactic space, performed the coregistration for Lead-DBS implementation, and contributed to the manuscript.

J.R.P. designed the study, acquired and analyzed the data, and contributed to the manuscript.

M.D.T. acquired and analyzed the data, and contributed to the manuscript.

J.A. designed the study, acquired and analyzed the data, and contributed to the manuscript.

J.P.S. advised on the building and testing of the coil, and contributed to the manuscript.

B.R.D. analyzed the data and contributed to the manuscript.

A.S. acquired and analyzed the data, and contributed to the manuscript.

L.S.T. processed and analyzed the data, and contributed to the manuscript.

R.D.F. performed the pathological assessment and contributed to the manuscript.

L.L.W. supervised the building of the coil and contributed to the manuscript.

B.F. supervised and designed the study, analyzed the data, and contributed to the manuscript.

A.v.d.K. supervised and designed the study, acquired and analyzed the data, and contributed to the manuscript.

Additional Information

Competing interests

None of the authors has a conflicting financial interest. Dr. Fischl and Mr. Tirrell have financial interest in CorticoMetrics, a company whose medical pursuits focus on brain imaging and measurement technologies. Their interests were reviewed and are managed by Massachusetts General Hospital and Partners HealthCare in accordance with their conflict of interest policies.

Figures

Figure 1. Human brain specimen. The human brain specimen that underwent *ex vivo* MRI is shown from inferior (**a**), superior (**b**), right lateral (**c**) and left lateral (**d**) perspectives. Gross pathological examination of the brain was normal.

Figure 2. Receive array coil and transmit volume coil for *ex vivo* imaging of the whole human brain. (**a**) The 31-channel receive array has 15 elements on the top half (with a diameter of 5.5 cm) and 16 on the bottom half (with a diameter of 8.5 cm), each made of 16 AWG wire loops with four or five evenly spaced capacitors. All elements are tuned to 297.2 MHz. (**c**) The coil former has slightly larger dimensions than the brain holder, which slides inside a volume coil (**b**). (**d**) A custom air-tight brain holder was designed to conform to the shape of a whole human brain. The brain holder is an oblate spheroid container (16 x 19 cm) with degassing ports that are used to apply a vacuum suction, thereby reducing air bubbles in the specimen and surrounding fomblin solution.

Figure 3. Comparison of FA25° acquisition and synthesized FLASH25 volume. Representative images from the FA25° acquisition (left column) and the synthesized FLASH25 volume (right column) are displayed in the sagittal (top row), coronal (middle row) and axial (bottom row) planes. These images provide a qualitative comparison of the respective signal-to-noise properties of

392   the FA25° acquisition (~25 hours) and the synthesized FLASH25 volume

393   (~100 hours). All images are shown in radiologic convention.

394

395   **Figure 4. Delineation of subcortical neuroanatomy.** Representative axial

396   sections from the synthesized FLASH25 volume are shown at the level of the

397   rostral pons and caudal midbrain (**a-c**, see inset in panel **c**). Zoomed views of

398   the brainstem, medial temporal lobe, and anterior cerebellum (within the white

399   rectangles in **a-c**) are shown in the bottom row (**d-f**). The anatomic detail that

400   can be visualized in this *ex vivo* 100 μm resolution MRI dataset is beyond that

401   which can be seen in typical *in vivo* MRI datasets. All images are shown in

402   radiologic convention. Neuroanatomic abbreviations: Amg = amygdala; Cb =

403   cerebellum; CP = cerebral peduncle; MB = mammillary body; P = pons; SCP =

404   superior cerebellar peduncle; VTA = ventral tegmental area; xSCP =

405   decussation of the superior cerebellar peduncle; Th = thalamus.

406

407   **Figure 5. Signal-to-noise ratio (SNR) analysis of coil performance.**

408   Representative SNR maps are shown in the sagittal (top row), coronal (middle

409   row) and axial (bottom row) planes for a test brain sample immersed in

410   periodate-lysine-paraformaldehyde. The maps demonstrate an SNR gain of

411   1.6-fold for the 31-channel 7 Tesla (7T) *ex vivo* coil (left column) compared to

412   the 31-channel 7T standard coil (middle row), and a gain of 3.3-fold compared

413   to the 64-channel 3T head coil (right column). The noise coupling between

414   channels was 11% for the 31-channel *ex vivo* coil array, a 2-fold improvement

415   relative to our previous array[18].

416

417 **Figure 6. Normalization of the *ex vivo* MRI dataset into standard**

418 **stereotactic space and integration into the Lead-DBS software platform.**

419 **(a)** Exemplary use-case of the normalized FLASH25 volume in deep brain

420 stimulation (DBS). DBS electrodes are visualized for a hypothetical patient

421 using Lead-DBS software (https://www.lead-dbs.org)[29]. An axial image from

422 the normalized scan, at the level of the rostral midbrain, is shown as a

423 backdrop, with 3D-structures defined by the DISTAL atlas[32] (right subthalamic

424 and left red nucleus hidden for optimal visualization of the underlying

425 anatomy). Panels (**b**) and (**c**) show zoomed views of key DBS target regions:

426 the left globus pallidus interna (GPi in **b**) and the subthalamic nucleus (STN in

427 **c**). The images in (**b**) and (**c**) are shown in radiologic convention.

References

428

429   1   Augustinack, J. C., van der Kouwe, A. J. & Fischl, B. Medial temporal

430   cortices in ex vivo magnetic resonance imaging. *J Comp Neurol* **521**,

431   4177-4188, doi:10.1002/cne.23432 (2013).

432   2   Edlow, B. L. *et al.* Neuroanatomic connectivity of the human ascending

433   arousal system critical to consciousness and its disorders. *J*

434   *Neuropathol   Exp   Neurol   **71**,   531-546,*

435   doi:10.1097/NEN.0b013e3182588293 (2012).

436   3   McNab, J. A. *et al.* The Human Connectome Project and beyond: Initial

437   applications of 300mT/m gradients. *Neuroimage* **80**, 234-245,

438   doi:10.1016/j.neuroimage.2013.05.074 (2013).

439   4   Roebroeck, A., Miller, K. L & Aggarwal, M. Ex vivo diffusion MRI of the

440   human brain: Technical challenges and recent advances. *NMR Biomed*

441   **32**, e3941, doi:10.1002/nbm.3941 (2019).

442   5   Aggarwal, M. *et al.* Feasibility of creating a high-resolution 3D diffusion

443   tensor imaging based atlas of the human brainstem: a case study at

444   11.7   T.   *Neuroimage*   **74**,   117-127,

445   doi:10.1016/j.neuroimage.2013.01.061 (2013).

446   6   Lusebrink, F., Sciarra, A., Mattern, H., Yakupov, R. & Speck, O. T1-

447   weighted in vivo human whole brain MRI dataset with an ultrahigh

448   isotropic resolution of 250 mum. *Sci Data* **4**, 170032,

449   doi:10.1038/sdata.2017.32 (2017).

450   7   Horn, A. *et al.* Teaching NeuroImages: In vivo visualization of Edinger

451   comb and Wilson pencils. *Neurology* **92**, e1663-e1664,

452   doi:10.1212/WNL.0000000000007252 (2019).

453   8   Takahashi, E., Song, J. W., Folkerth, R. D., Grant, P. E. &

454   Schmahmann, J. D. Detection of postmortem human cerebellar cortex

455   and white matter pathways using high angular resolution diffusion

456   tractography: a feasibility study. *Neuroimage* **68**, 105-111,

457   doi:10.1016/j.neuroimage.2012.11.042 (2013).

458   9   Augustinack, J. C. *et al.* Detection of entorhinal layer II using 7Tesla

459   [corrected] magnetic resonance imaging. *Ann Neurol* **57**, 489-494,

460   doi:10.1002/ana.20426 (2005).

461   10   Gangolli, M. *et al.* Quantitative validation of a nonlinear histology-MRI

462   coregistration method using generalized Q-sampling imaging in

463   complex human cortical white matter. *Neuroimage* **153**, 152-167,

464   doi:10.1016/j.neuroimage.2017.03.059 (2017).

465   11   van Veluw, S. J. *et al.* Microbleed and microinfarct detection in amyloid

466   angiopathy: a high-resolution MRI-histopathology study. *Brain* **139**,

467   3151-3162, doi:10.1093/brain/aww229 (2016).

468   12   Sengupta, S. *et al.* High resolution anatomical and quantitative MRI of

469   the entire human occipital lobe ex vivo at 9.4T. *Neuroimage* **168**, 162-

470   171, doi:10.1016/j.neuroimage.2017.03.039 (2018).

471   13   van der Kouwe, A. *et al.* High Resolution Structural and Diffusion MRI

472   of Ex Vivo Human Motor Cortex. *Organization for Human Brain*

473   *Mapping* (2011).

474   14   Mareyam, A. *et al.* Array coil and sample preparation and support

475   system for whole brain ex vivo imaging at 100 μm. *ISMRM. #3130*

476   (2015).

477   15   Edlow, B. L. *et al.* Multimodal Characterization of the Late Effects of

478   Traumatic Brain Injury: A Methodological Overview of the Late Effects

of Traumatic Brain Injury Project. *J Neurotrauma* **35**, 1604-1619, doi:10.1089/neu.2017.5457 (2018).

16   Bridgers, L. D. *Design and Manufacture of an Ultra-High Field Ex Vivo Coil Assembly*, Massachusetts Institute of Technology, (2012).

17   Keil, B. *et al.* Size-optimized 32-channel brain arrays for 3 T pediatric imaging. *Magn Reson Med* **66**, 1777-1787, doi:10.1002/mrm.22961 (2011).

18   Mareyam, A., Polimeni, J. R., Alagappan, V., Fischl, B. & Wald, L. L. A 30 channel receive-only 7T array for ex vivo brain hemisphere imaging. *ISMRM. #106* (2009).

19   Fischl, B. *et al.* Sequence-independent segmentation of magnetic resonance images. *Neuroimage* **23 Suppl 1**, S69-84, doi:10.1016/j.neuroimage.2004.07.016 (2004).

20   Frigo, M. & Johnson, S. G. The Design and Implementation of FFTW3. *Proceedings of the IEEE* **93**, 216-231 (2005).

21   Deoni, S. C., Peters, T. M. & Rutt, B. K. High-resolution T1 and T2 mapping of the brain in a clinically acceptable time with DESPOT1 and DESPOT2. *Magn Reson Med* **53**, 237-241, doi:10.1002/mrm.20314 (2005).

22   Tovi, M. & Ericsson, A. Measurements of T1 and T2 over time in formalin-fixed human whole-brain specimens. *Acta Radiol* **33**, 400-404 (1992).

23   Eickhoff, S. *et al.* High-resolution MRI reflects myeloarchitecture and cytoarchitecture of human cerebral cortex. *Hum Brain Mapp* **24**, 206-215, doi:10.1002/hbm.20082 (2005).

23

504   24   Fukunaga, M. *et al.* Layer-specific variation of iron content in cerebral

505   cortex as a source of MRI contrast. *Proc Natl Acad Sci U S A* **107**,

506   3834-3839, doi:10.1073/pnas.0911177107 (2010).

507   25   Stuber, C. *et al.* Myelin and iron concentration in the human brain: a

508   quantitative study of MRI contrast. *Neuroimage* **93 Pt 1**, 95-106,

509   doi:10.1016/j.neuroimage.2014.02.026 (2014).

510   26   Fonov, V. S., Evans, A. C., McKinstry, R. C., Almli, C. R. & Collins, D.

511   Unbiased nonlinear average age-appropriate brain templates from birth

512   to adulthood. *Neuroimage* **47**, S102 (2009).

513   27   Horn,   A.   PCA   MNI   2009b   NLIN   template.   (2017).

514   <doi:10.6084/m9.figshare.4644472.v2>.

515   28   Avants, B. B., Epstein, C. L., Grossman, M. & Gee, J. C. Symmetric

516   diffeomorphic image registration with cross-correlation: evaluating

517   automated labeling of elderly and neurodegenerative brain. *Medical*

518   *image analysis* **12**, 26-41, doi:10.1016/j.media.2007.06.004 (2008).

519   29   Horn, A. *et al.* Lead-DBS v2: Towards a comprehensive pipeline for

520   deep   brain   stimulation   imaging.   *Neuroimage*   **184**,   293-316,

521   doi:10.1016/j.neuroimage.2018.08.068 (2019).

522   30   Kellman, P. & McVeigh, E. R. Image reconstruction in SNR units: a

523   general method for SNR measurement. *Magn Reson Med* **54**, 1439-

524   1447, doi:10.1002/mrm.20713 (2005).

525   31   Yarnykh, V. L. Actual flip-angle imaging in the pulsed steady state: a

526   method for rapid three-dimensional mapping of the transmitted

527   radiofrequency   field.   *Magn   Reson   Med*   **57**,   192-200,

528   doi:10.1002/mrm.21120 (2007).

24

529   32   Ewert, S. *et al.* Toward defining deep brain stimulation targets in MNI

530   space: A subcortical atlas based on multimodal MRI, histology and

531   structural   connectivity.   *Neuroimage*   **170**,   271-282,

532   doi:10.1016/j.neuroimage.2017.05.015 (2018).

533

Data Citations

534

535   1. Edlow, B.L., Mareyam, A., Horn, A., Polimeni, J.R., Tisdall M.D.,

536   Augustinack, J., Stockmann, J.P., Diamond B.R., Stevens, A., Tirrell, L.,

537   Folkerth, R.D., Wald, L.L., Fischl, B. & Kouwe, A.v.d. *Dryad Digital*

538   *Repository.* https://datadryad.org. doi:10.5061/dryad.119f80q (2019).

539

540   *2.* Edlow, B.L., Mareyam, A., Horn, A., Polimeni, J.R., Tisdall M.D.,

541   Augustinack, J., Stockmann, J.P., Diamond B.R., Stevens, A., Tirrell, L.,

542   Folkerth, R.D., Wald, L.L., Fischl, B. & Kouwe, A.v.d. *Biolucida*

543   https://histopath.nmr.mgh.harvard.edu (2019).

544

545   3. Edlow, B.L., Mareyam, A., Horn, A., Polimeni, J.R., Tisdall M.D.,

546   Augustinack, J., Stockmann, J.P., Diamond B.R., Stevens, A., Tirrell, L.,

547   Folkerth, R.D., Wald, L.L., Fischl, B. & Kouwe, A.v.d. *Lead-DBS*

548   https://www.lead-dbs.org (2019).

549

Videos

Video 1. Axial images from the FA25˚ acquisition. These images were acquired in ~25 hours of scan time. The images are shown in radiologic convention.

Video 2. Coronal images from the FA25˚ acquisition. These images were acquired in ~25 hours of scan time. The images are shown in radiologic convention.

Video 3. Sagittal images from the FA25˚ acquisition. These images were acquired in ~25 hours of scan time.

Video 4. Axial images from the synthesized FLASH25 volume. These images were acquired in ~100 hours of scan time. The images are shown in radiologic convention.

Video 5. Coronal images from the synthesized FLASH25 volume. These images were acquired in ~100 hours of scan time. The images are shown in radiologic convention.

Video 6. Sagittal images from the synthesized FLASH25 volume. These images were acquired in ~100 hours of scan time.
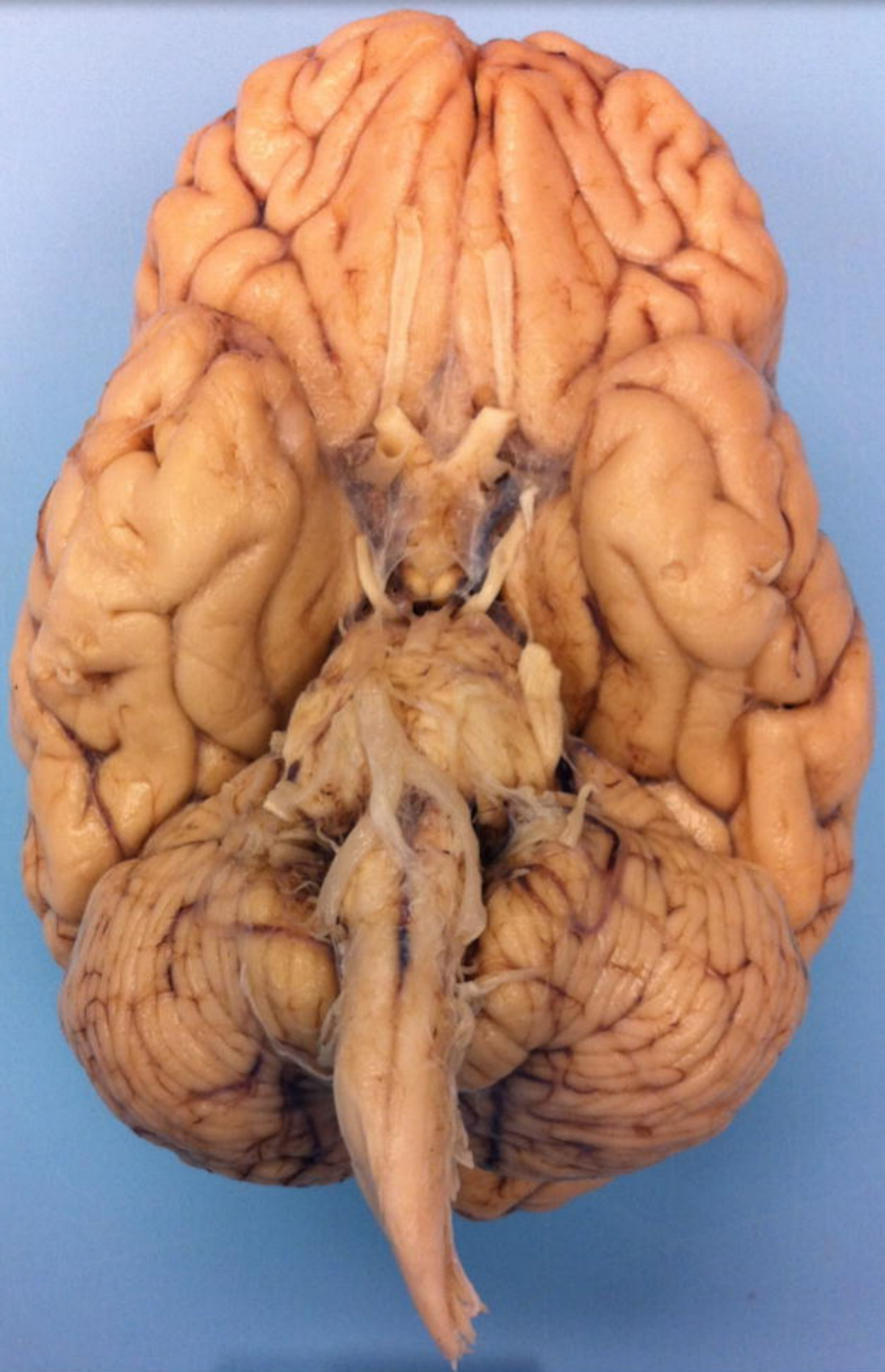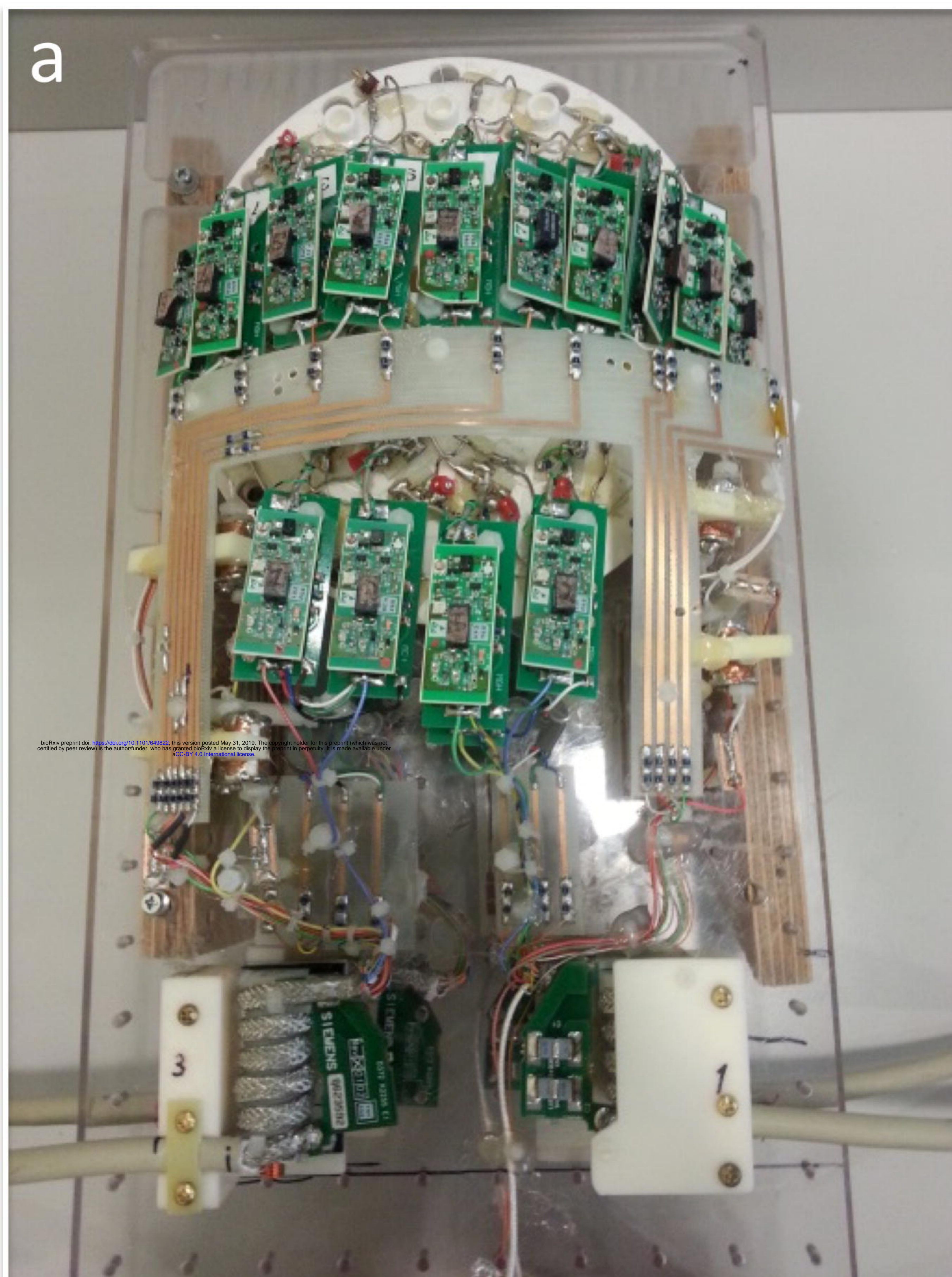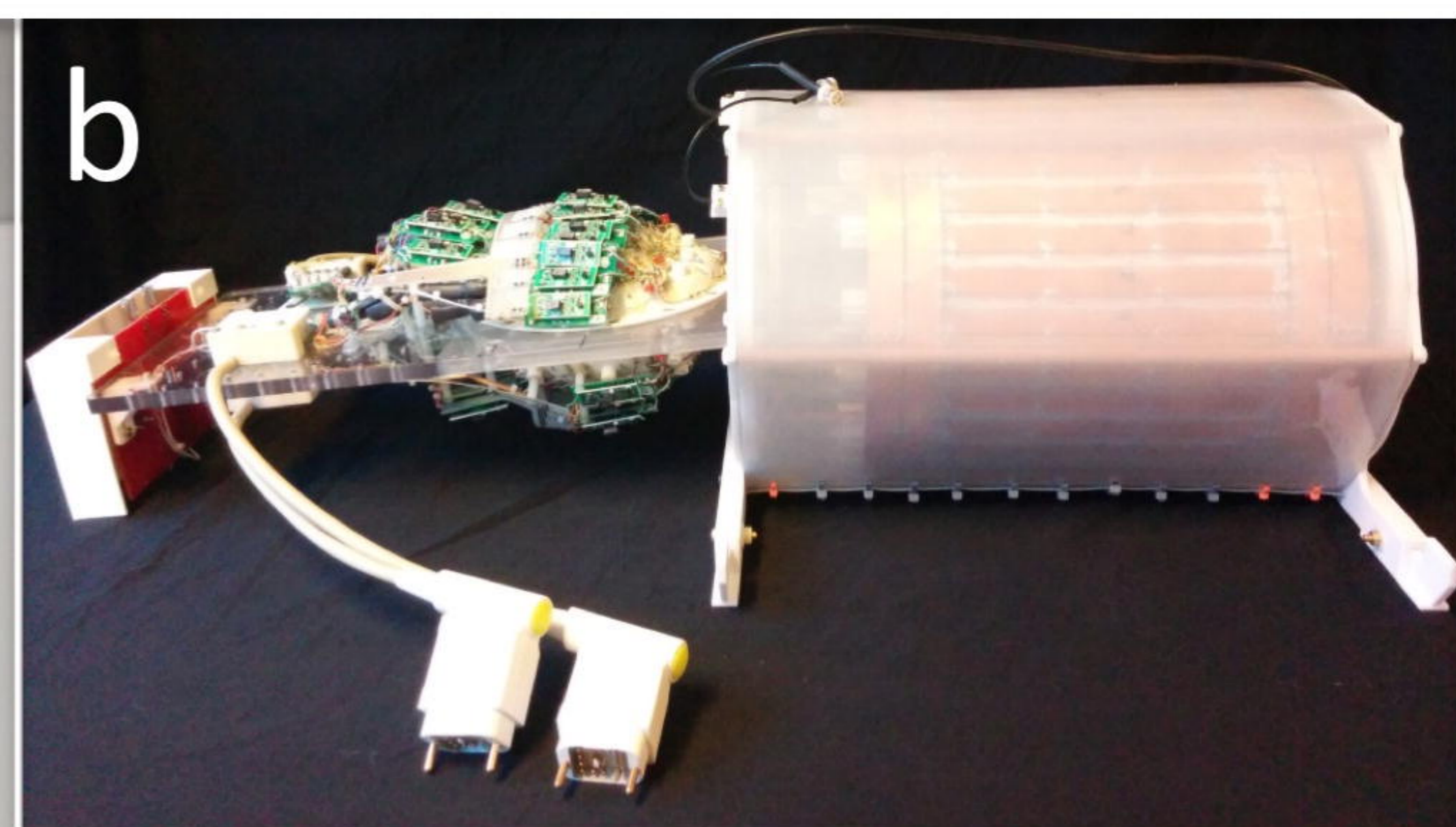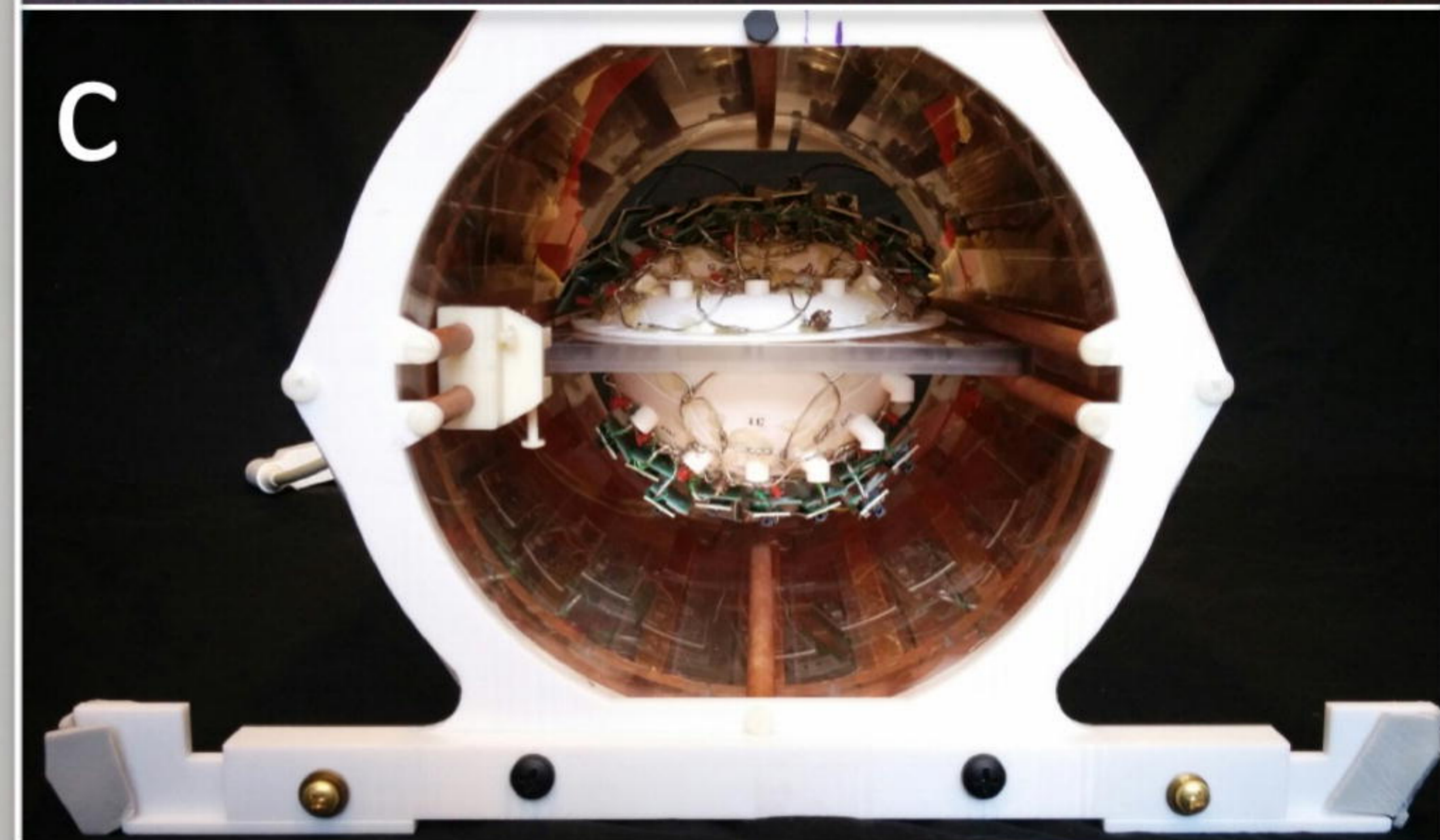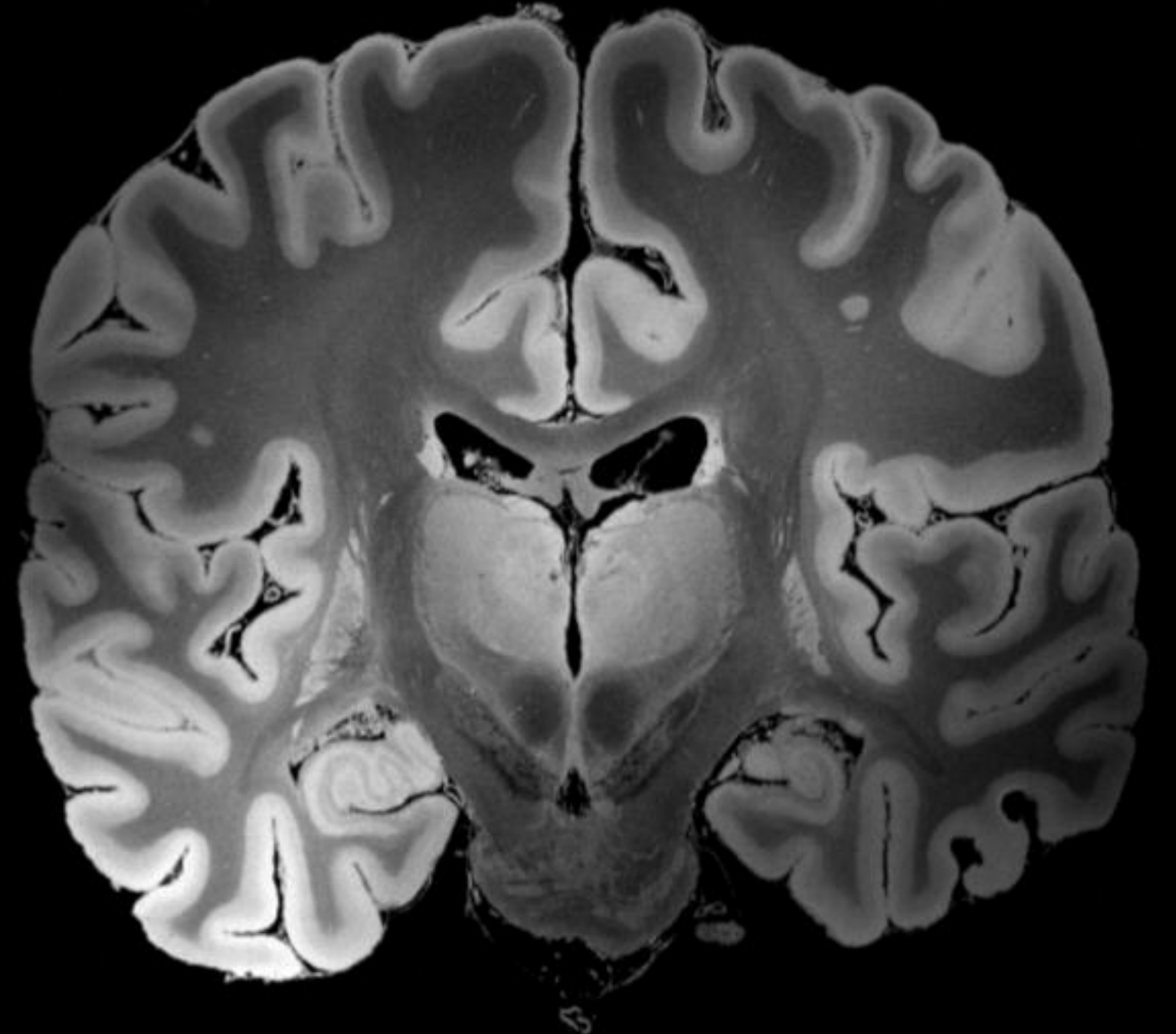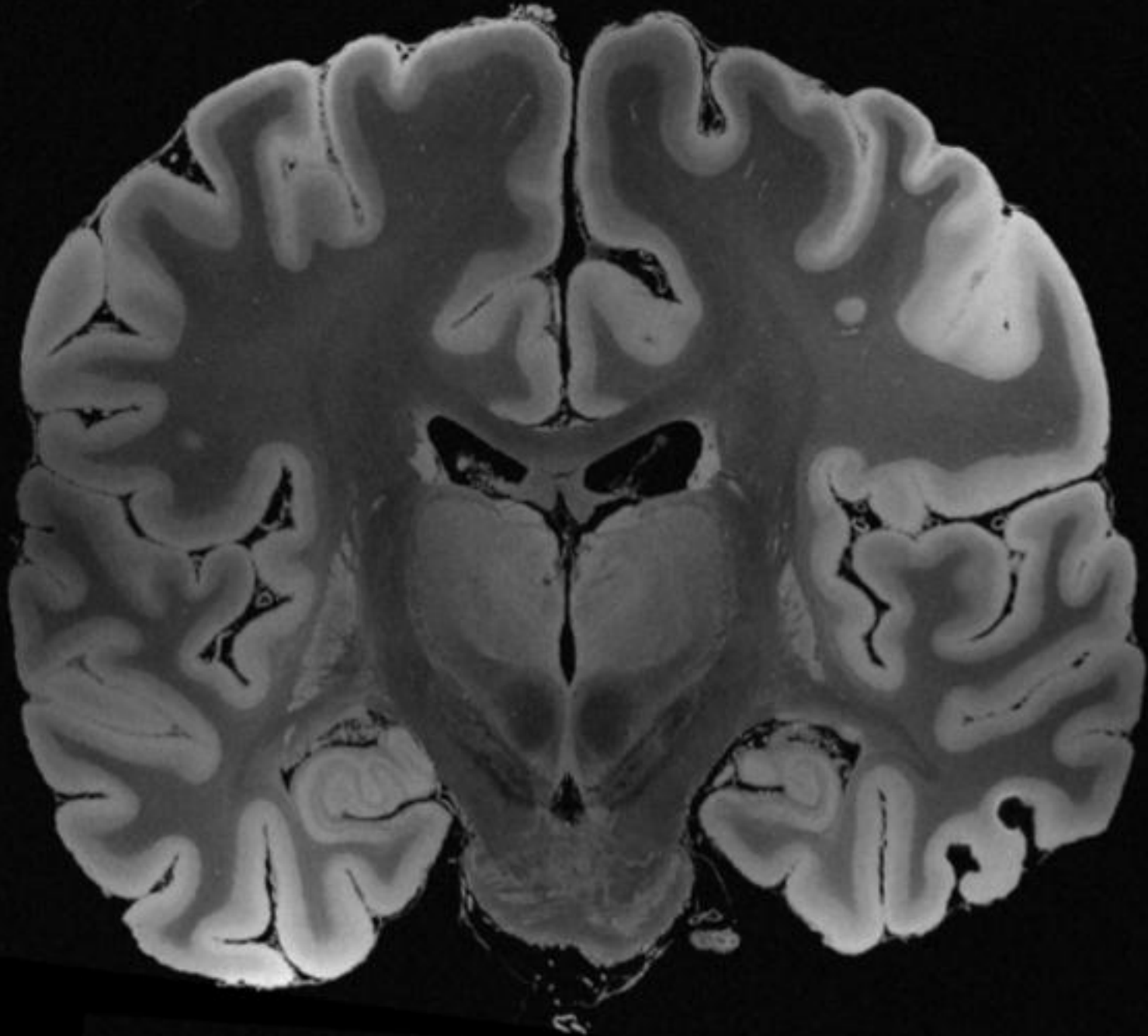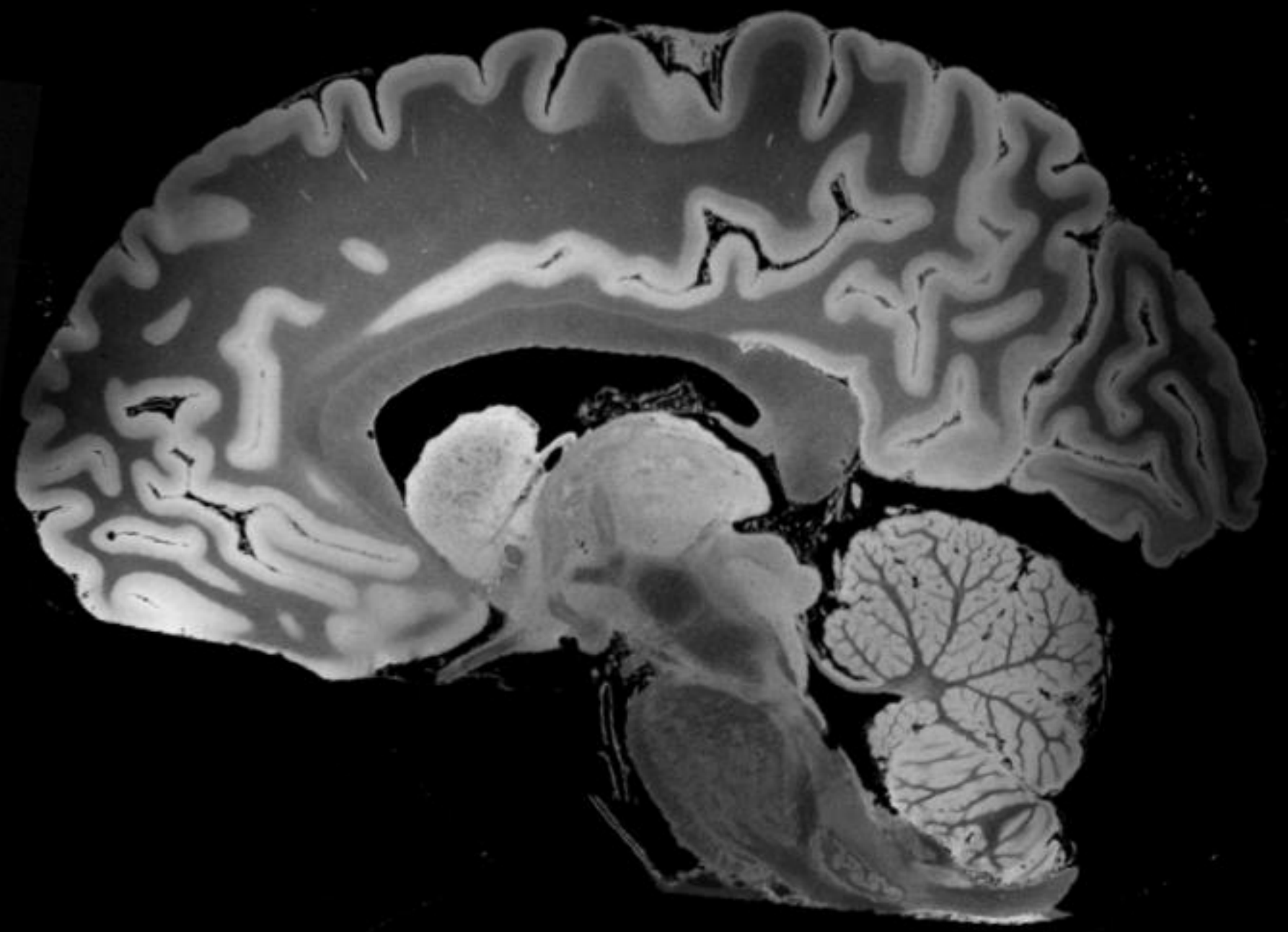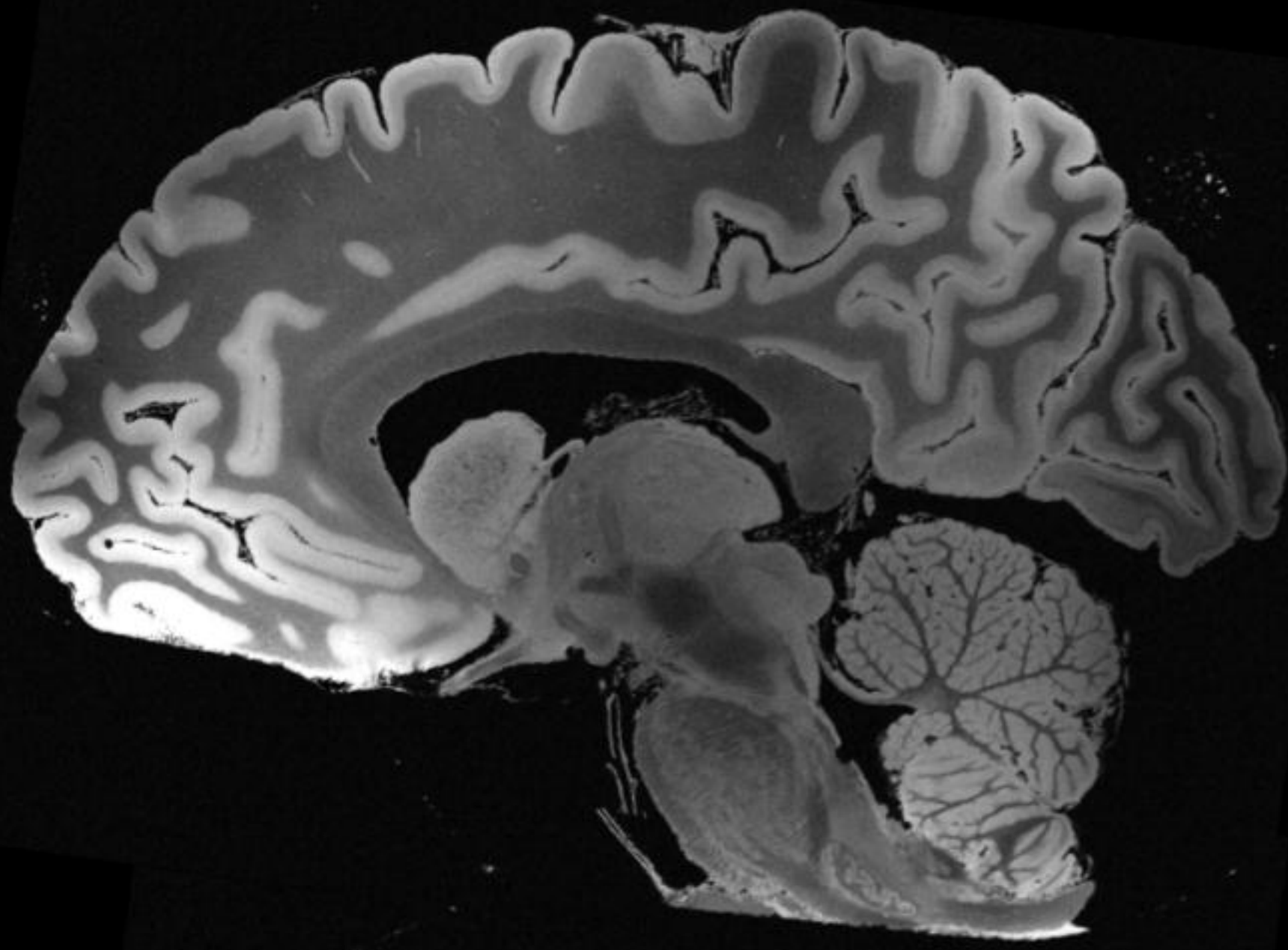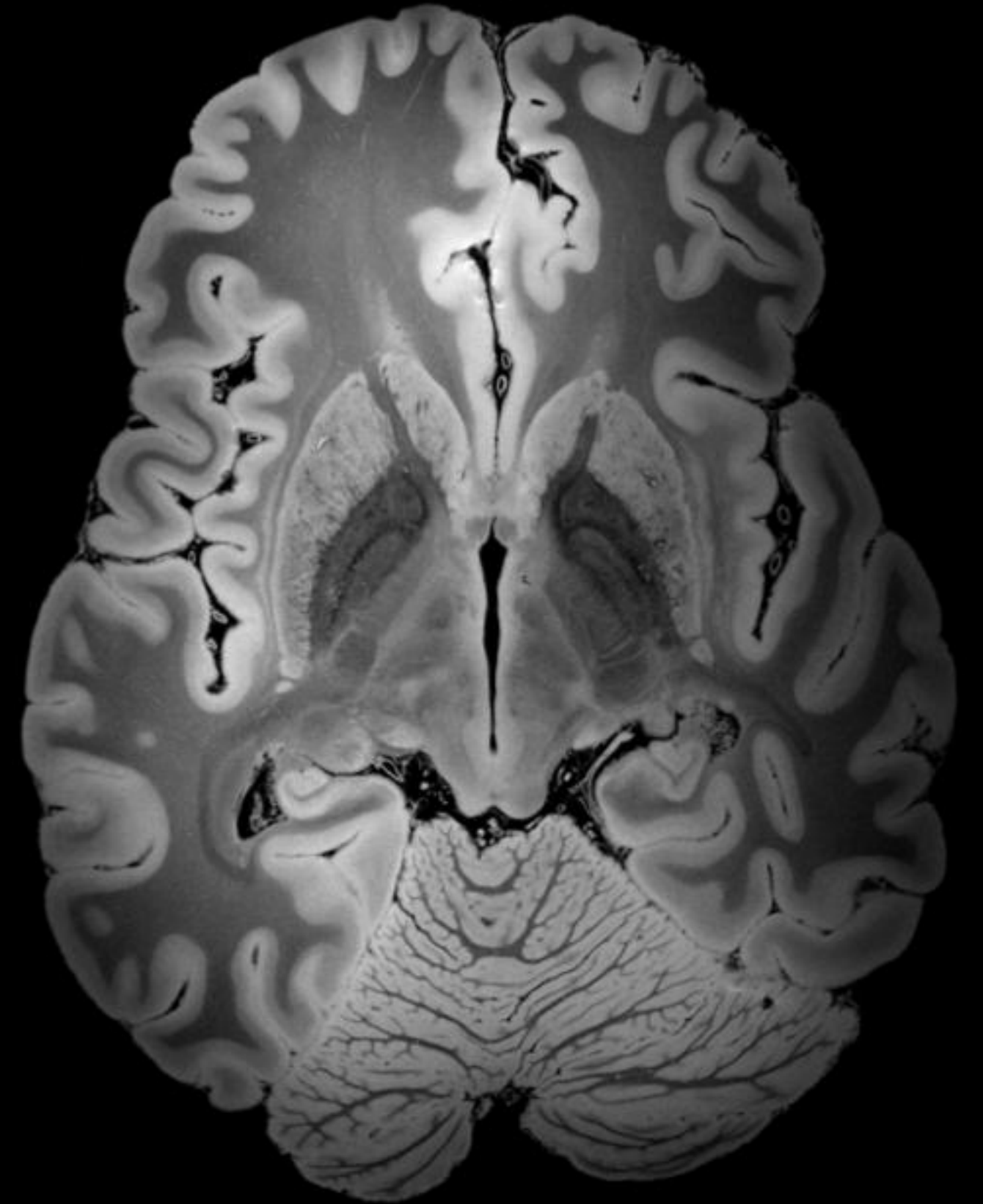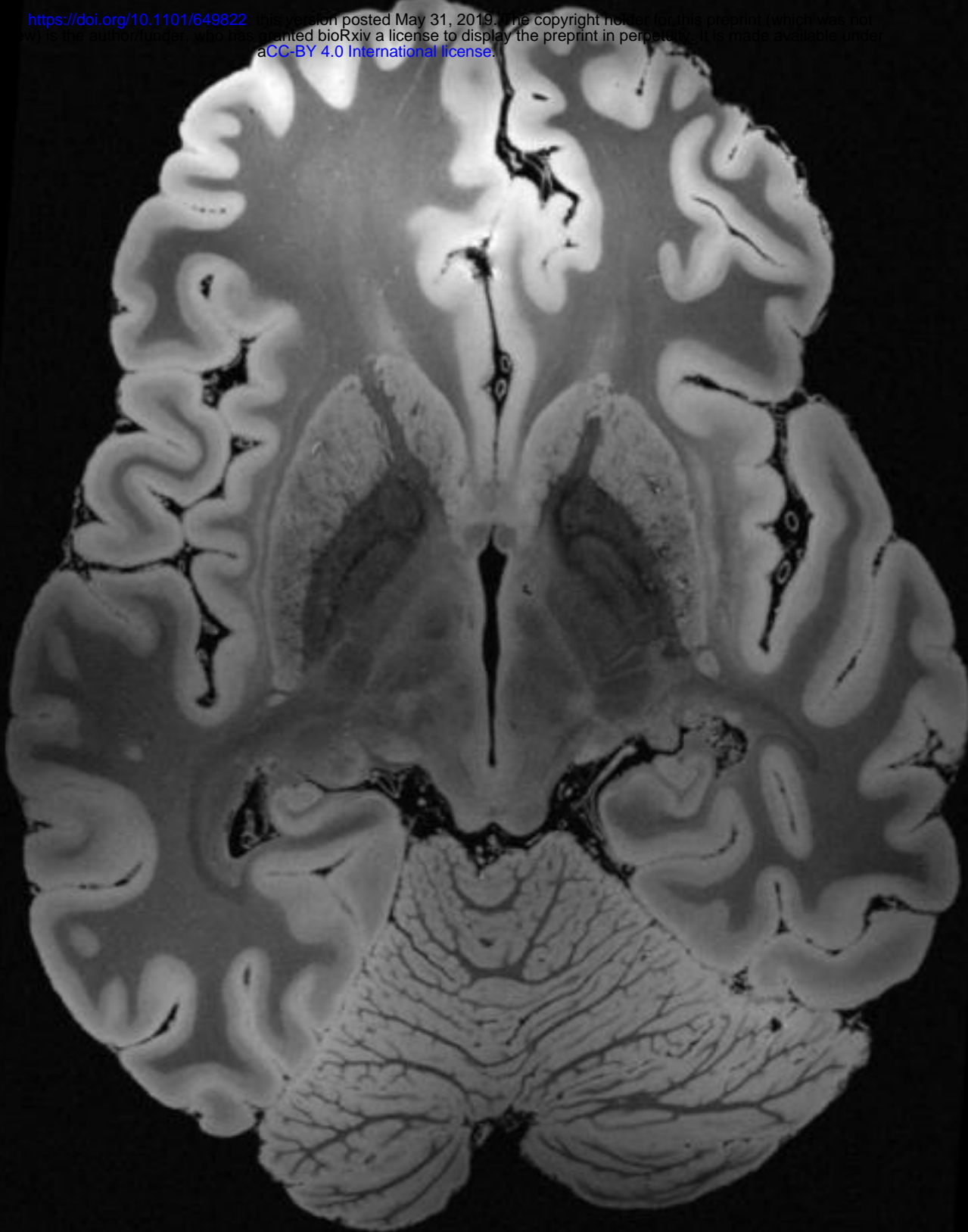
Acquired FA25°
(~25 hours)

Synthesized FLASH25
(~100 hours)
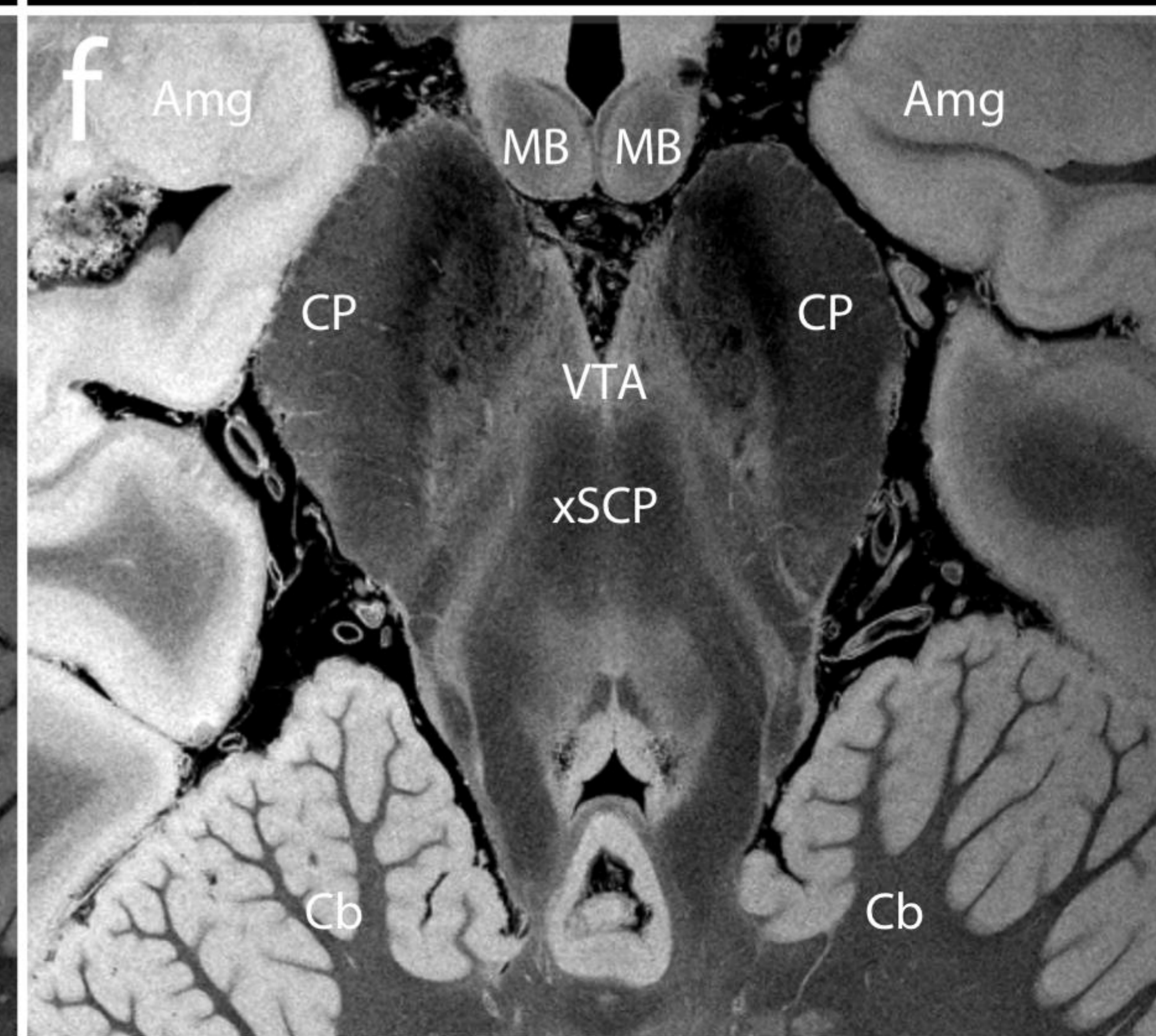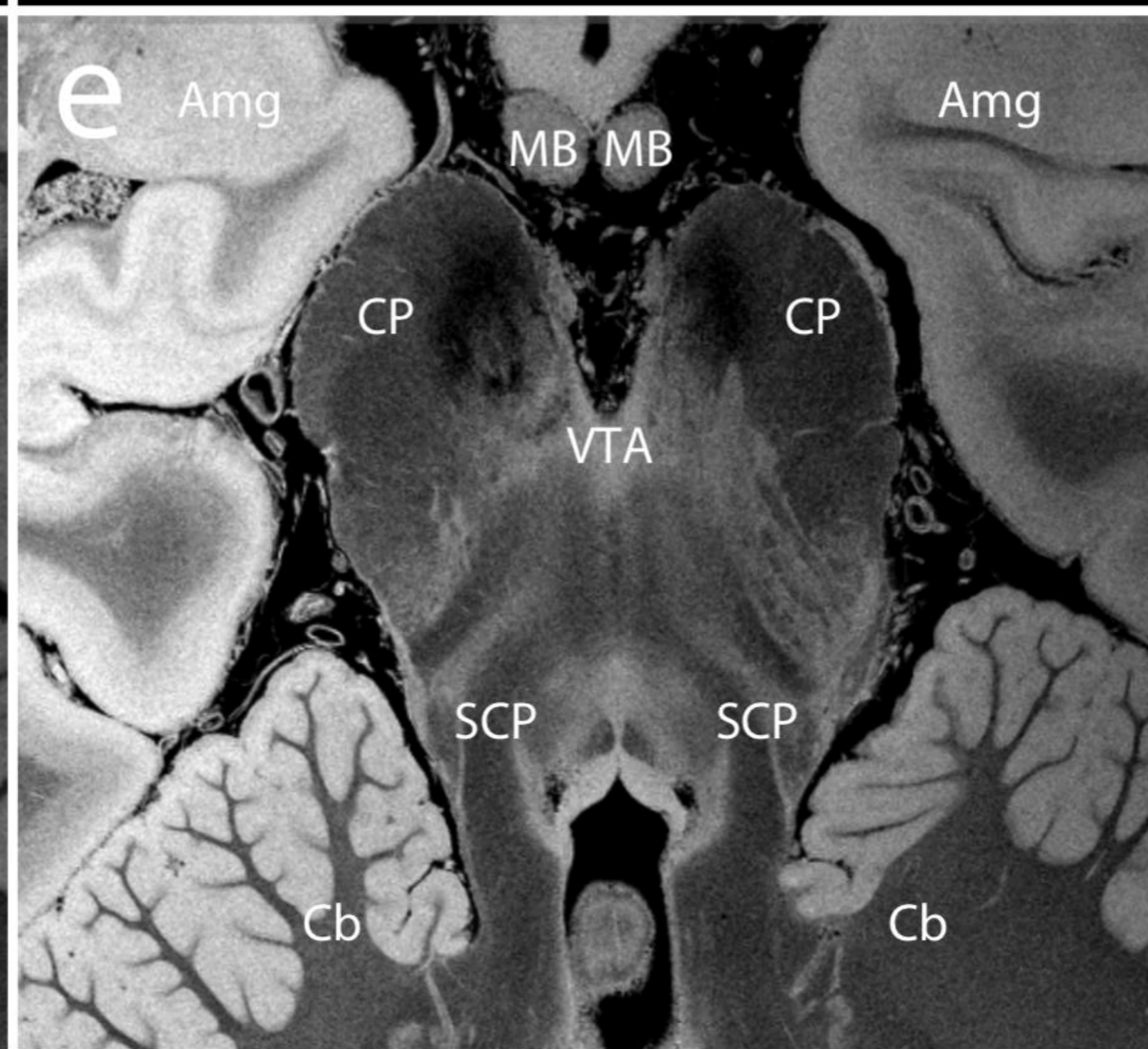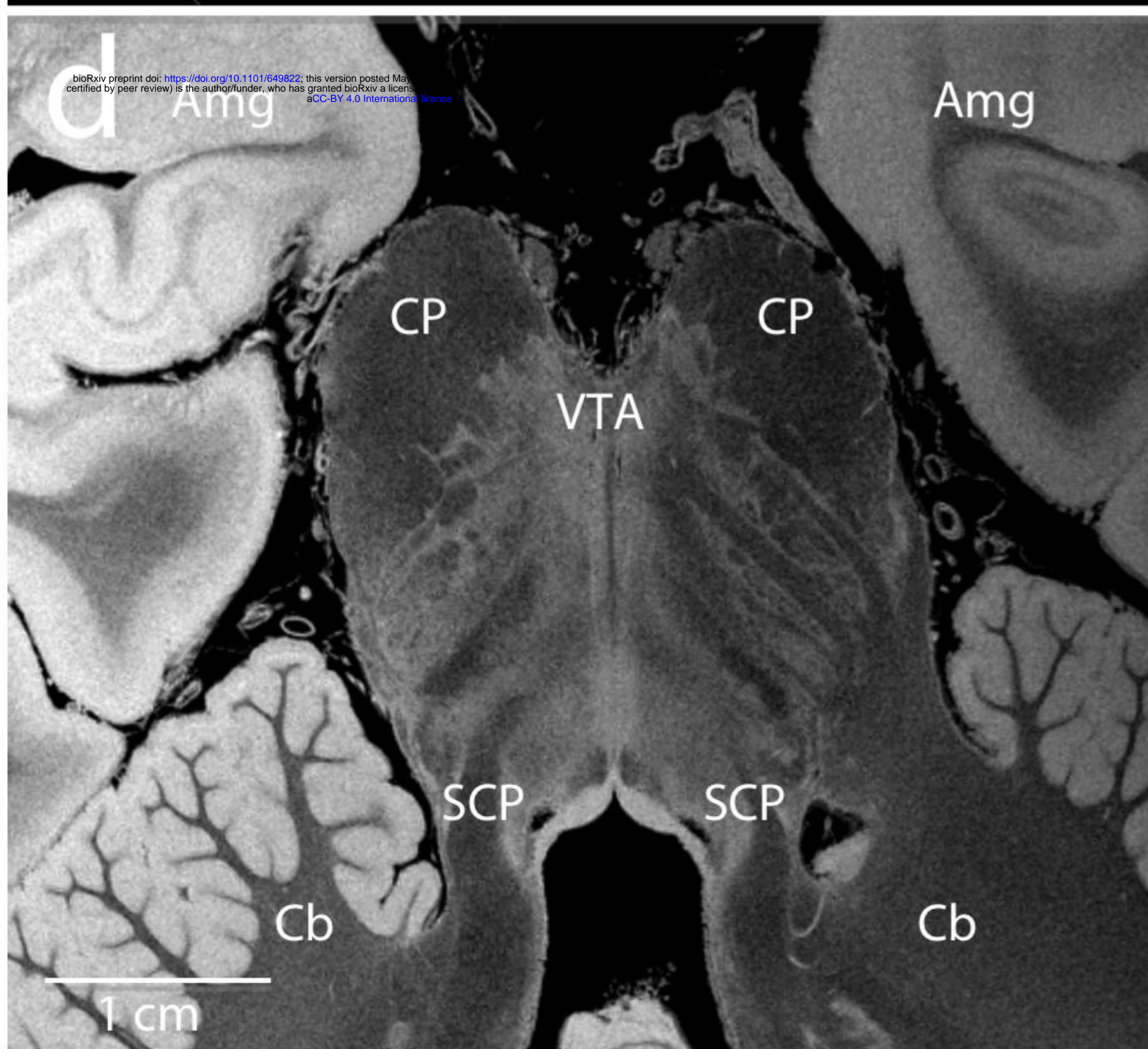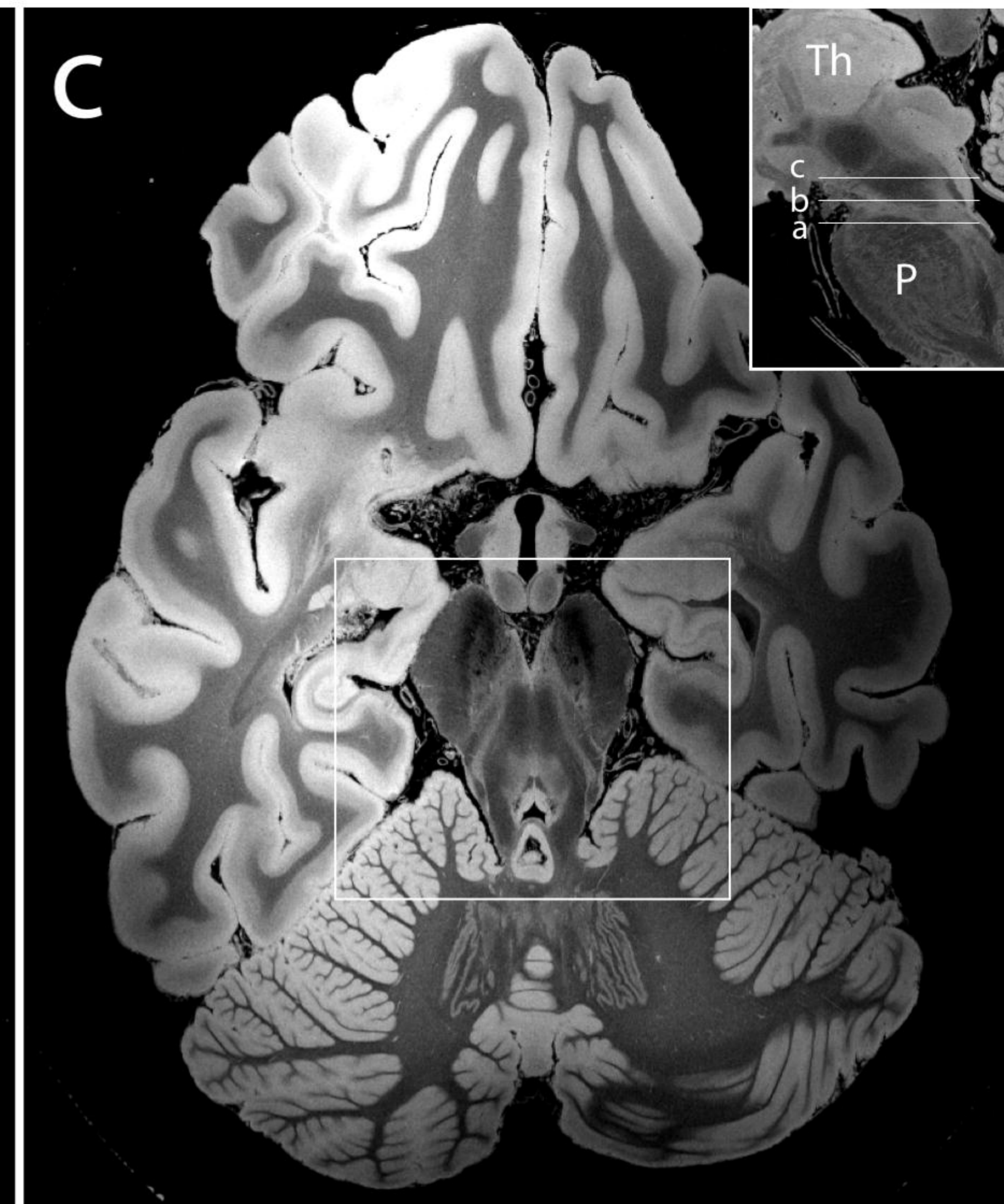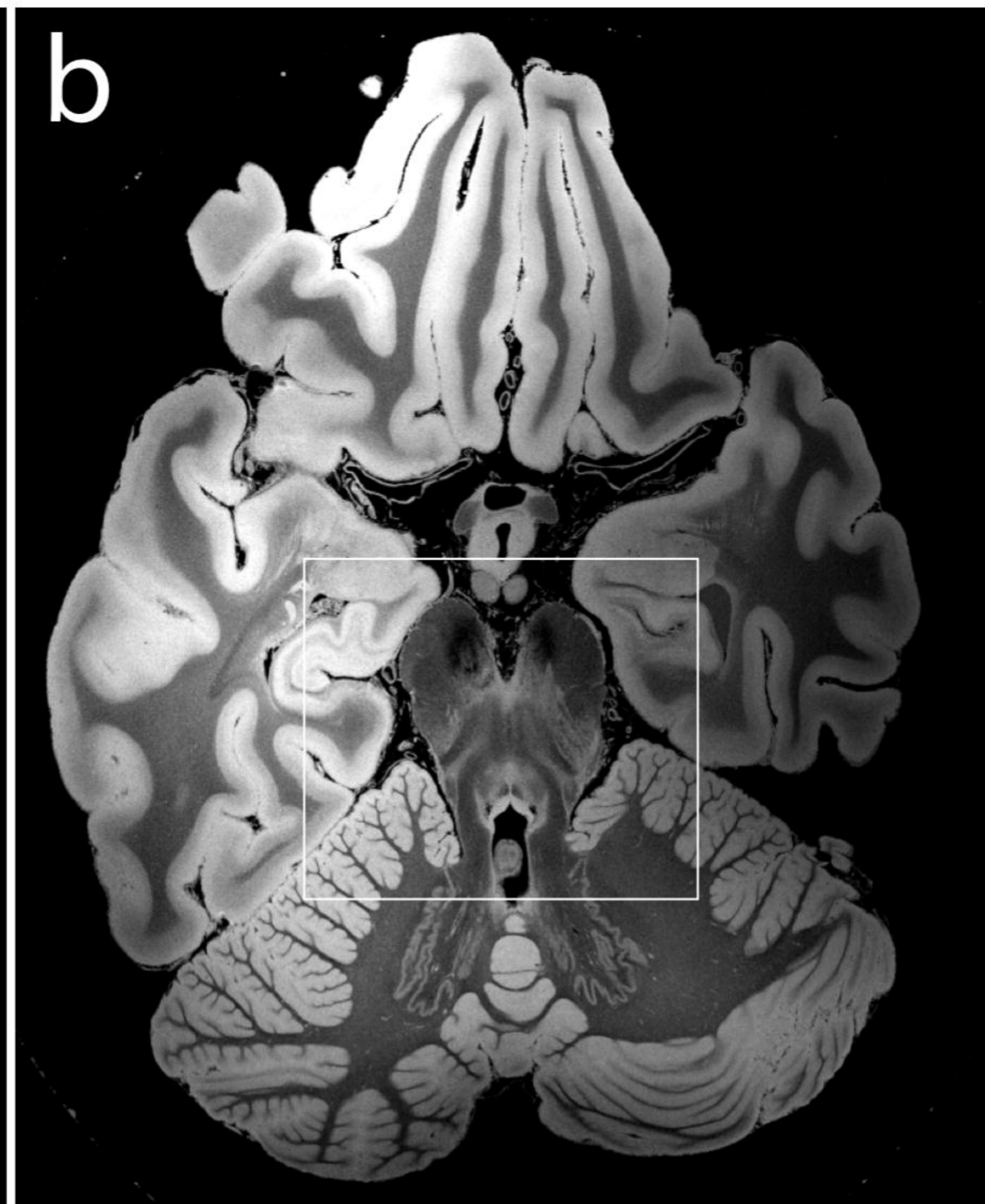
	7T 31Ch *ex vivo* coil	7T 31Ch standard coil	3T 64Ch head coil
Sagittal			
Coronal			
Axial			

SNR Units

a

PUTAMEN

EXTERNAL

INTERNAL
PALLIDUM

CAUDATE

RED NUCLEUS

SUBTHALAMIC
NUCLEUS

COMB
SYSTEM

b

GPi

c

STN